Supplementary Information: Low-dimensional Dynamics of Two Coupled Biological Oscillators
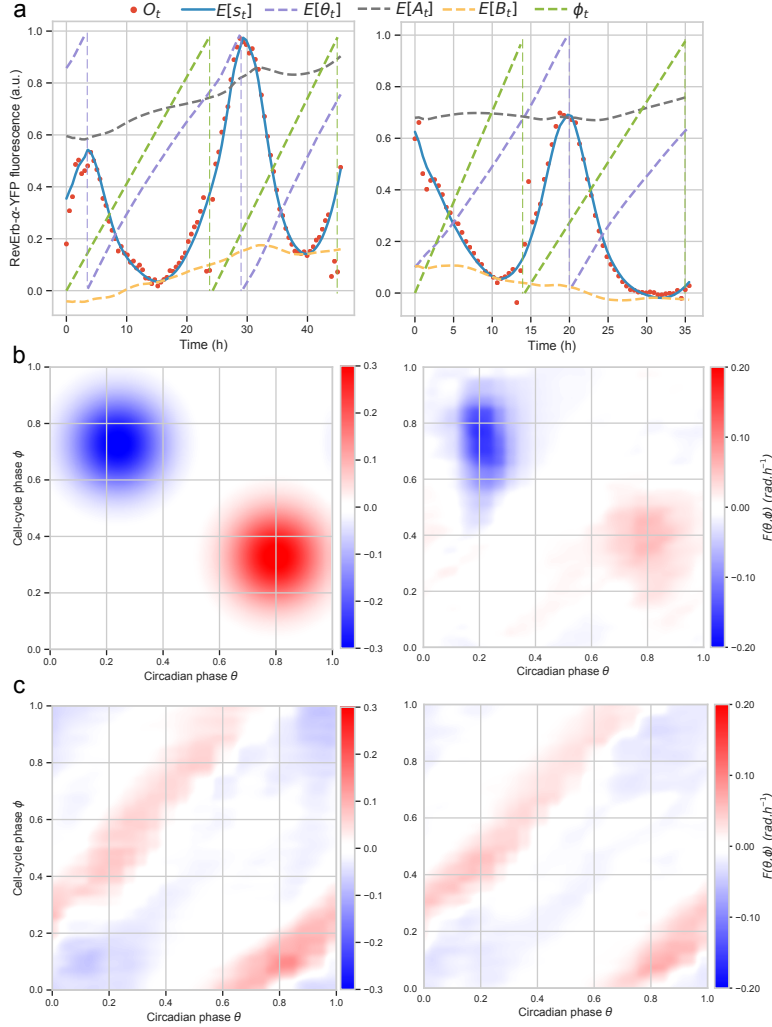
Colas Droin, Eric R. Paquet, Felix Naef

# Contents

Part I
Supplementary Figures & Movies

Supplementary Figure 1: Validation of the inference method. (**a**) Examples of temporal data traces and model fits. The colors show data (red), posterior mean for S_t (blue), posteriors circular mean for θ_t (dashed purple), posterior means A_t (dashed grey) and baseline B_t (dashed yellow). The cell-cycle phase ϕ_t (which is not a hidden variable) is obtained from linear interpolation between two successive divisions (dashed green line). Deviations of the purple curve from a straight line corresponds to transient variations of circadian phase velocity, owing to noise and coupling. (**b-c**) Using oscillator parameters mimicking real cells, we can recover coupling functions from simulated traces. (**b**) First, we simulated traces with a coupling $F(\theta, \phi)$ comprising two Gaussian interaction regions, as shown in the left panel. The reconstructed function is shown in the right panel. (**c**) Same numerical experiment made with the coupling inferred from the real data as input (left). Both simulations reveal that the inferred functions are qualitatively accurate, but quantitatively damped.
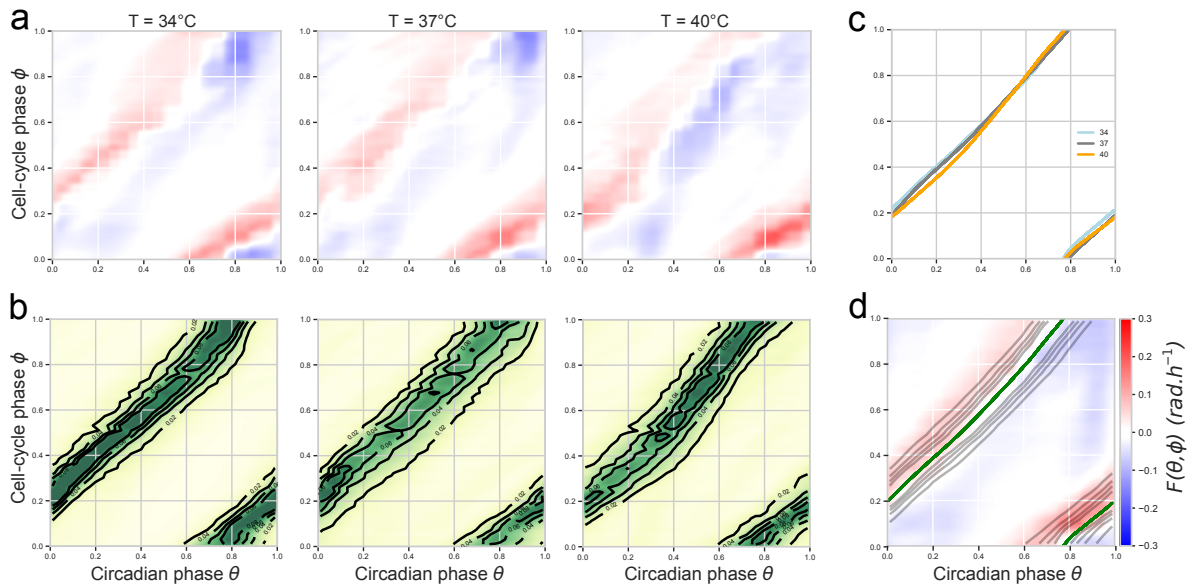
Supplementary Figure 2: $F(\theta, \phi)$ **depends weakly on temperature.** (**a**) Coupling functions obtained from traces acquired at 34°C, 37°C and 40°C. Here, to avoid possible bias, the traces were sampled such that the distribution of cell-cycle periods is identical for each temperature (n = 513 in each case, Supplementary Fig. 3a for the cell-cycle period distributions at the three different temperatures). (**b**) Superimposition of the merged (from all traces at 34°C, 37°C, and 40°C) coupling function (that of Fig. 2a), the phase-space trace density (Fig. 2b, here shown as contour lines), and the attractor (Fig. 2c, green line). (**c**) Attractors for the vector fields in a) show that the 1:1 phase-locked orbit is temperature independent. (**d**) Phase space densities obtained in the same condition and from the same traces as in (**a**).
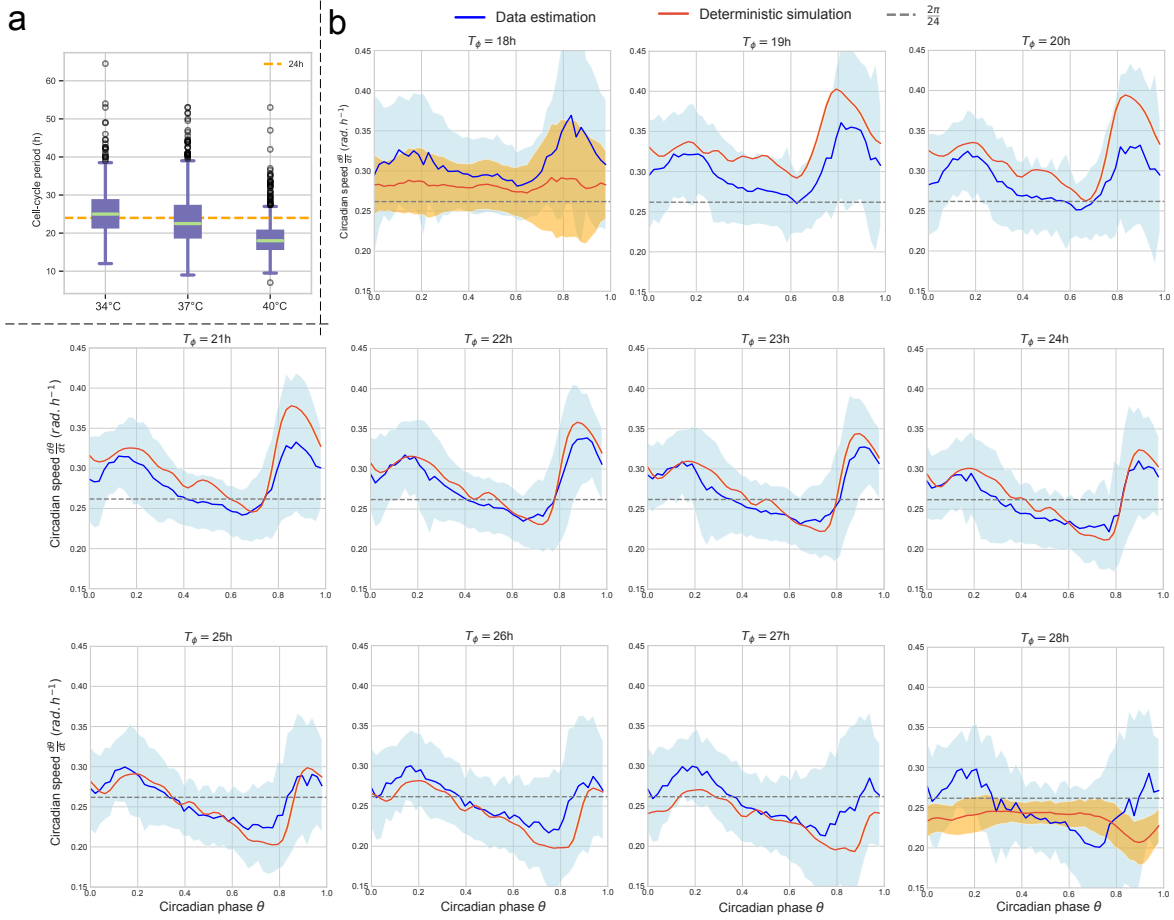
Supplementary Figure 3: The phase velocity profiles along the 1:1 attractors in function of cell-cycle period. (**a**) Cell-cycle period (division-to-division time intervals) distributions in NIH3T3 cells at three temperatures. The average period progressively decreases from around 24h at 34°C to 18h at 40°C. (**b**) Circadian phase velocity on the 1:1 attracting orbit in function of cell-cycle period (increasing from left to right and top to bottom). The phase velocity shown is either inferred from the data traces (blue line, standard deviation in light blue), or simulated using the deterministic model (no phase noise) (orange line). The first and last panels ($T_\phi = 18$h and 28h) have quasi-periodic orbits (hence a standard deviation is associated with the mean phase velocity). The natural (non-dividing cells) circadian phase velocity (about $0.26\ rad.h^{-1}$, corresponding to a 24h period) is indicated by a dashed grey line.
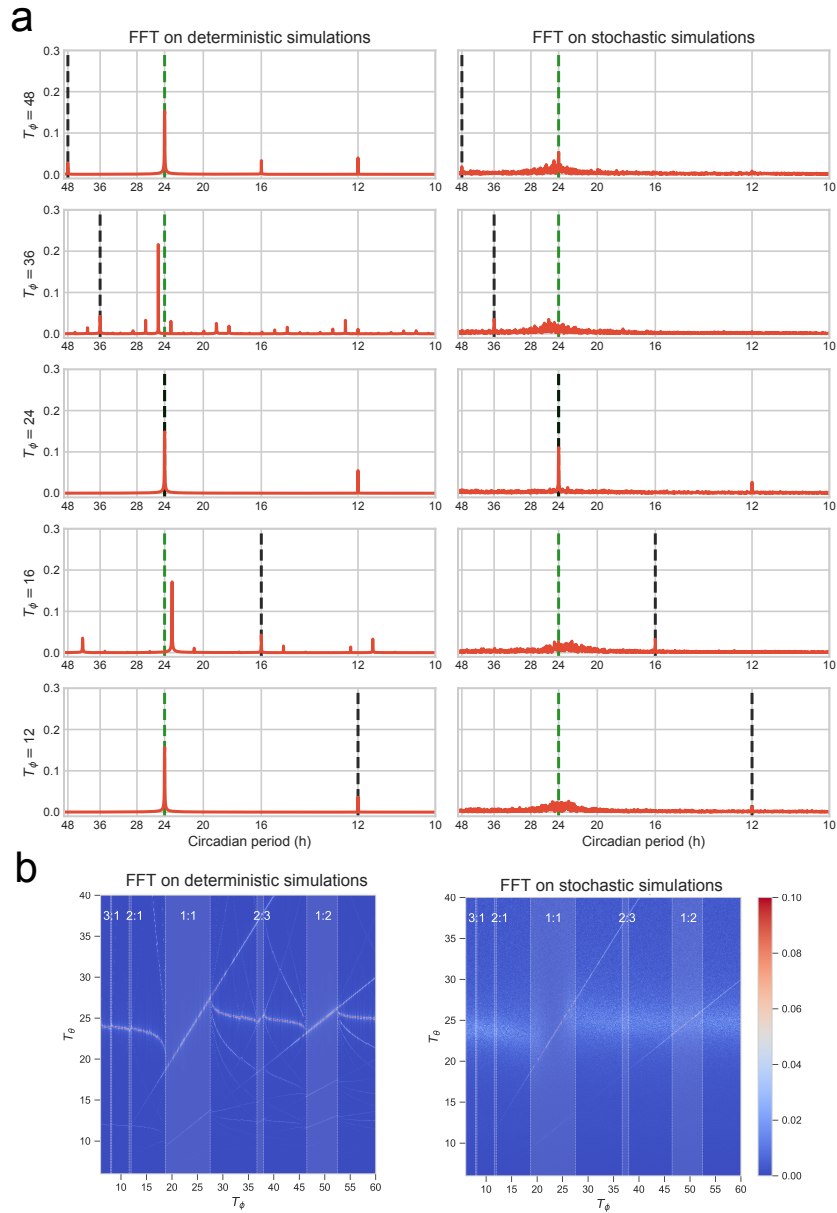
Supplementary Figure 4: Spectral analysis of simulated traces shows that 1:1 phase-locking is robust against noise. (**a**) Spectral analysis of long simulated circadian traces (total simulation length: 10.000h) using either the deterministic (left, phase diffusion set to zero) or stochastic (right) model, for different cell-cycle periods. Periods of the natural circadian period (24h, green dashed line), and that of the entraining cell cycle (black dashed lines) are indicated. (**b**) Power spectra presented in (**a**) shown as heatmaps for 350 different cell-cycle periods (see also Movie 3). Phase-locked intervals are observed in the deterministic model (left) as lines for the fundamental and few harmonics. Only 1:1 and the 1:2 are visible in the presence of noise (right).
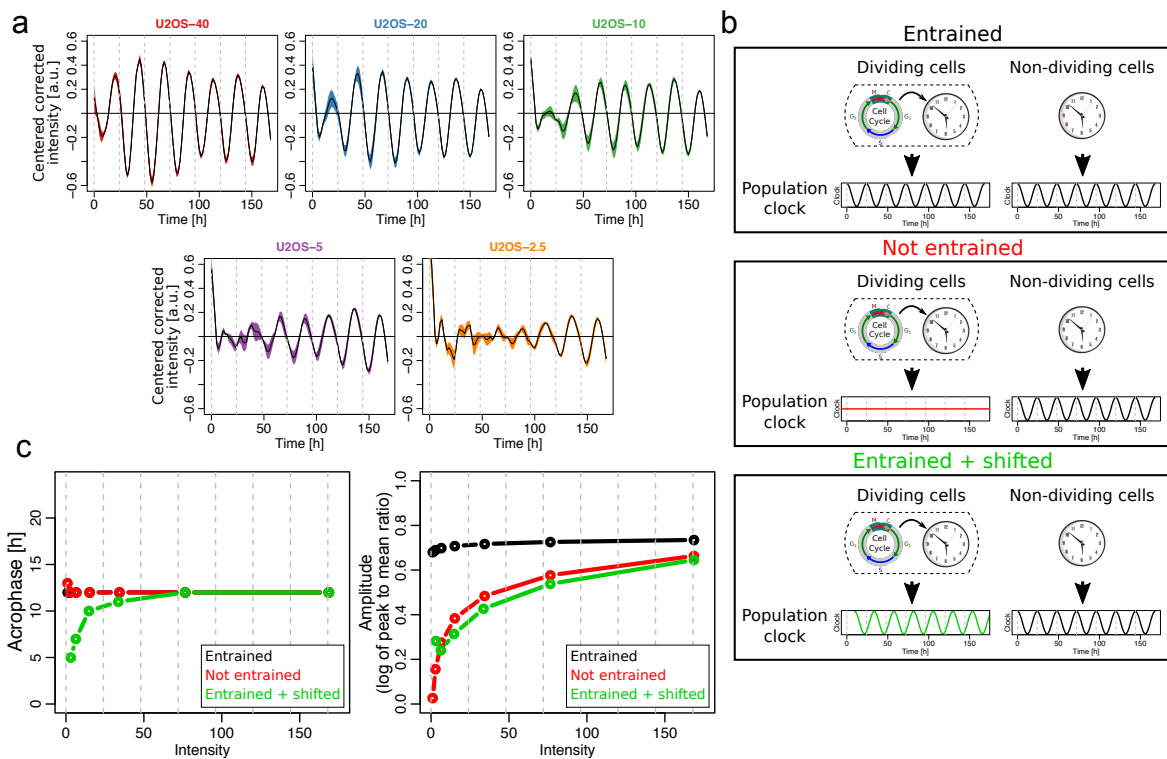
Supplementary Figure 5: The circadian clock of dividing cells does not entrain to temperature cycles. (**a**) Averaged (n=6) Bmal1-Luc intensities and 95% confidence intervals from U2OS-Dual Bmal1 luciferase signal centered and corrected for temperature artifact (Supplementary Information). Results were obtained by plating different number of cells (40k, 20k, 10k, 5k, or 2.5k) at the beginning of the experiment. (**b**) Pictograms depicting three different models: i) the circadian oscillators in dividing cells adopt the same circadian profile as non-dividing entrained cells; ii) are not entrained; or iii) are entrained, but with a different phase compared to non-dividing cells. (**c**) Acrophase (hour of the peak of the signal) (left) and amplitude (log of peak to mean ratio) (right) in function of intensity obtained from simulations of the three models in b). Results here should be compared with Figure 6b in the main text.

Movie 1: Single-cell trajectories of circadian and cell-cycle phases cluster around a 1:1 phase-locked state. Inferred temporal single-cell trajectories in the phase-space. Each cell is represented by a point, and its instantaneous direction by a tail. The color shows the instantaneous phase velocity of the circadian phase of the cell is blue or red depending in the instantaneous speed is respectively slower of faster than the intrinsic circadian clock speed ($\frac{2\pi}{24} rad.h^{-1}$). The phase density is progressively built in the background from the accumulation of the cell trajectories.

Movie 2: Simulations of the deterministic model shows phase-locking and quasi-periodicity. Vector fields and simulated (deterministic) trajectories for increasing cell-cycle periods T_ϕ. Simulations in forward time are represented with a green line, while simulations in backward time are represented with a red. The vector field (in blue) shows the instantaneous phase velocities. Phase-locked states, interspersed with quasi-periodic orbits, are successively observed. The beginnings of trajectories are removed to show steady-states.

Movie 3: Spectral analysis of the deterministic and stochastic simulations shows qualitative differences in function of the cell-cycle period. Animated representation of Supplementary Figure 4 for increasing cell-cycle velocity. The instantaneous position of the system on the Arnold tongues is represented by a red dot.

Part II

Supplementary Methods

1 Reconstruction of the dynamical model

The main objective is to perform a data-driven reconstruction of a stochastic models for the coupled systems of circadian and cell cycles, and to then analyze the consequences on the coupled oscillator dynamics. A key step is to estimate the coupling function $F(\theta, \phi)$ (expressed in terms of the phases of the two oscillators) representing the influence of the cell-cycle on the circadian clock.

Our approach consists in explicitly modeling the measured fluorescent signals, using a set of stochastic ordinary differential equations (SODEs) whose parameters are estimated by maximizing the probability of observing the data over the entire set of cell traces. Parameters of the SODEs, which include the oscillator coupling, are assumed to be shared by all cells of a given experimental condition. The method uses several steps, which are detailed in the following sections.

1.1 Stochastic models for the oscillator phases and measured signals

1.1.1 Phase model for dividing cells

The circadian phase, representing the state of the circadian oscillator of an individual cell, is modeled as a diffusion-drift process, while the cell-cycle has simpler, piece-wise linear dynamics between two divisions. This is motivated by previous work where we have shown that the influence of the clock on the cell-cycle was very weak, and probably nonexistent [1]. Therefore we focus here on a precise characterization of the coupling function representing the cell-cycle influence on the clock, and then study the dynamical implications.

We first introduce some notation. $\theta, \phi \in [0; 2\pi[\times [0; 2\pi[$ represent the phases of the circadian clock and the cell-cycle, respectively. The intrinsic period of the circadian clock, T_θ, is kept fixed to $24h$, while the cell-cycle intervals T_ϕ^i are indexed on the division-to-division interval i. The coupling function $F(\theta, \phi)$ represents the influence of the cell-cycle phase on the circadian clock phase. σ_θ is the noise strength of the circadian phase, the noise itself being modelled through a Wiener process $W_{\theta,t}$. The stochastic phase model is a two-dimensional diffusion drift written as follows:

$$\begin{cases} \mathrm{d}\theta_t = \frac{2\pi}{T_\theta}\mathrm{d}t + F(\theta_t, \phi_t)\mathrm{d}t + \sigma_\theta\,\mathrm{d}W_{\theta,t} \\ \mathrm{d}\phi_t = \frac{2\pi}{T_\phi^i}\mathrm{d}t \end{cases} \tag{1}$$

1.1.2 Phase model for non-dividing cells

Due to inherent fluctuations in biological processes, there are always cells in a dish which transiently exit the cell cycle. On the other hand, the circadian cycle proceeds unperturbed also in quiescent cells. For such cell traces without division, we assume that the model for

8

the circadian phase reduces to just one stochastic ordinary differential equation:

$$\mathrm{d}\theta_t = \frac{2\pi}{T_\theta}\mathrm{d}t + \sigma_\theta \mathrm{d}W_{\theta,t} \tag{2}$$

containing the parameters of the bare oscillator. In fact we will use such traces to estimate those parameters (see 1.2.1).

1.1.3 Model for the fluorescence signals

The experimental signals obtained from microscopy show noisy oscillations with variations in the amplitude of the maxima as well as in the fluorescence background. For convenience, we centered and rescaled all single cell traces such that the 5th percentile is 0 and 95th percentile is 1.

The phase θ_t is linked to the signal S_t via a function $w(\theta_t)$, which thus defines the phase in our model. In order to use a common definition of the phase, in particular one that does not depend on temperature or cell type (*i.e.* NIH3T3 and U2OS cells), we estimated a single function $w(\theta_t)$, as the the average of all peak-to-peak signals of non-dividing cells. This showed that indeed NIH3T3 and U2OS cells yield very similar functions, and we therefore used the average as a fixed function for all analyses (Fig. 6).
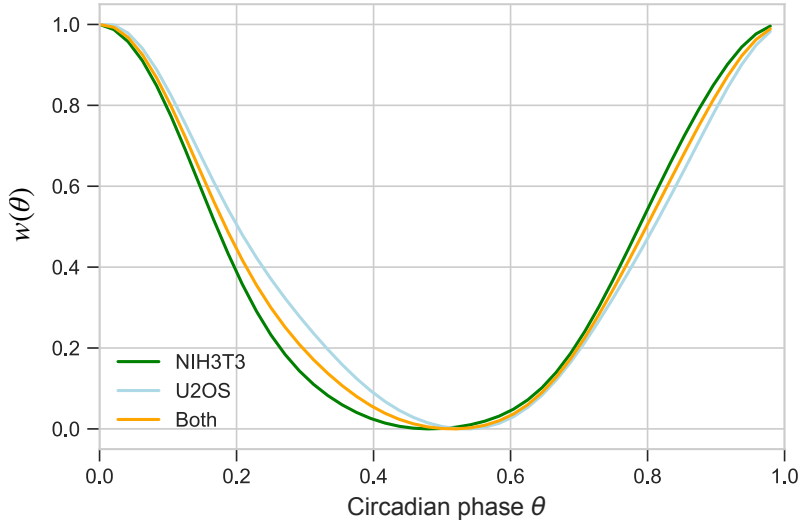
Figure 6: Estimated $w(\theta)$ from NIH3T3 (green) and U2OS (blue) traces reveal little difference between them. To keep a consistent definition for the phase, the final function was taken as the average (yellow).

To take into account the variations of amplitude and background, two Ornstein-Uhlenbeck (O-U) processes are used: A_t and B_t, modelled as stochastic ordinary differential equations:

$$\begin{cases} \mathrm{d}A_t = -\gamma_A(A_t - \mu_A)\mathrm{d}t + \sigma_A\,\mathrm{d}W_{A,t} \\ \mathrm{d}B_t = -\gamma_B(B_t - \mu_B)\mathrm{d}t + \sigma_B\,\mathrm{d}W_{B,t} \\ S_t = \exp(A_t)w(\theta_t) + B_t + \xi \end{cases} \tag{3}$$

In this parametrization, the stationary mean and variance are $E[X_t] = \mu_X$ and $Var[X_t] = \frac{\sigma_X^2}{2\gamma_X}$, for $X = A, B$, respectively. ξ represents additional experimental (measurement) white noise with zero mean and variance σ_e^2.

This model assumes that the amplitude and the background fluctuations are independent from the phase (see Section 1.3 in this document).

1.1.4 Conversion of the model into a Hidden Markov Model (HMM)

A HMM is defined as a stochastic triplet $\boldsymbol{\Omega} = \{\boldsymbol{\pi}, \boldsymbol{A}, \boldsymbol{E}\}$, where $\boldsymbol{\pi}$ is the vector containing the initial probability distribution of the modeled Markov process, and the matrices $\mathbf{A}$ and $\mathbf{E}$ contain the transition and emission probabilities of the process [2].

To define the transition and emission matrices, we first discretize the model. The discrete phase, amplitude and background domains are defined as:

$$\begin{cases} \boldsymbol{\Psi} = \{k\Delta_\Psi | k \in \{0, 1, ..., N-1\}, \Delta_\Psi = 2\pi/N\} = \{\psi_0, ..., \psi_{N-1}\} \\ \boldsymbol{\mathcal{A}} = \{A_{min} + k\Delta_A | k \in \{0, 1, ..., M-1\}, \Delta_A = \frac{A_{max}-A_{min}}{M}\} = \{a_0, ..., a_{M-1}\} \\ \boldsymbol{\mathcal{B}} = \{B_{min} + k\Delta_B | k \in \{0, 1, ..., M-1\}, \Delta_B = \frac{B_{max}-B_{min}}{M}\} = \{b_0, ..., b_{M-1}\} \end{cases} \quad , \quad (4)$$

with N and M the numbers of hidden states for the phase and the O-U processes, respectively.

The maxima (A_{max}, B_{max}) and minima (A_{min}, B_{min}) are chosen at least three standard deviations away from the mean of the corresponding O-U processes. The full hidden state space is then $\boldsymbol{\mathcal{X}} = \boldsymbol{\Psi} \times \boldsymbol{\mathcal{A}} \times \boldsymbol{\mathcal{B}}$.

The transition probabilities are then obtained from the following:

$$p(\theta_{t+dt}|\theta_t = \psi_i, \phi_t = \psi_j) = N\left(\psi_i + \frac{2\pi}{T_\theta}dt + F(\psi_i, \psi_j)dt, \sigma_\theta^2 dt\right) \quad , \quad (5)$$

where we have made the approximation that dt is small.

For the O-U processes, the results are well-known [3]:

$$p(A_{t+dt}|A_t = a_i) = N\left(\mu_A + (a_i - \mu_A)e^{-\gamma_A dt}, (1 - e^{-2\gamma_A dt})\frac{\sigma_A^2}{2\gamma_A}\right) \quad , \quad (6)$$

$$p(B_{t+dt}|B_t = b_i) = N\left(\mu_B + (b_i - \mu_B)e^{-\gamma_B dt}, (1 - e^{-2\gamma_B dt})\frac{\sigma_B^2}{2\gamma_B}\right) \quad , \quad (7)$$

All the transitions between the three processes are assumed to be independent:

$$\mathbf{A}_{ijk,lm,no} = p_{tr}(\psi_k|\psi_i, \psi_j)P_{tr}(a_m|a_l)P_{tr}(b_o|b_n) \ . \quad (8)$$

Finally, the probability of an observation O_t obeys to:

$$p(O_t|A_t = a_i, B_t = b_j, \theta_t = \psi_k) = \frac{1}{\sigma_e\sqrt{2\pi}}e^{-\frac{1}{2}\left(\frac{\exp(a_i)w(\psi_k)+b_j-O_t}{\sigma_e}\right)^2} \ . \quad (9)$$

Note that w appears in this equation, enabling to compare the prediction of the model with the actual observations. Also note that in this SI we use O_t to refer to a specific observation in our dataset, instead of S_t in the generic case. However, both notations are interchangeable.

10

The emission matrix $\boldsymbol{E_t}$ for each time point can then be computed as:

$$\boldsymbol{E}_{t,ijk} = p_e(O_t|a_i, b_j, \psi_k) \ . \tag{10}$$

The fixed cell-cycle phases, given at each time point through a linear interpolation are noted as $\boldsymbol{\Phi}$, such that $\boldsymbol{\Phi} = \{\phi_0, \ldots, \phi_t, \ldots, \phi_T\}$ with $\phi_t \in \boldsymbol{\Psi} \forall t$.

Once the matrices $\boldsymbol{\pi}, \boldsymbol{A}$ and $\boldsymbol{E}$ are built, one can compute the probability of a state $\mathbf{x} \in \mathcal{X}$ given all the observations $\mathbf{O} = \{O_1, ..., O_t, ..., O_T\}$, that is the posterior state distribution $p(\mathbf{x}|\mathbf{O})$, using the forward-backward algorithm [2]. A graphical representation of the HMM is is provided Figure 7.
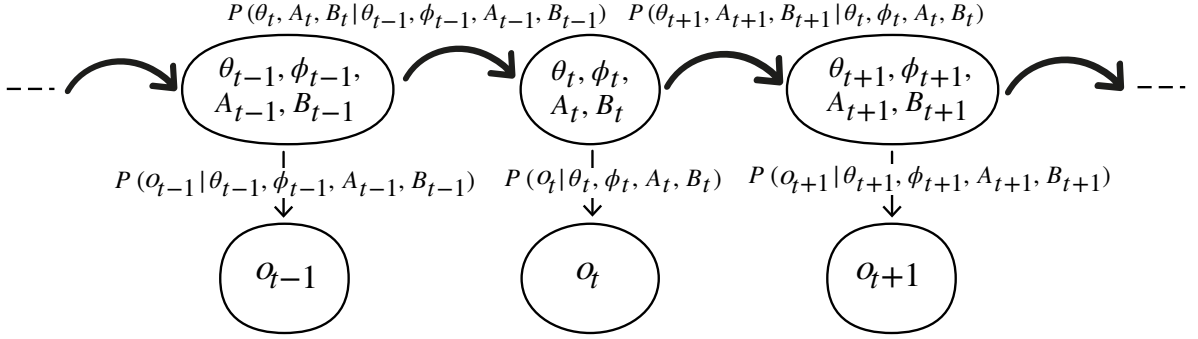

Figure 7: Representation of the Hidden Markov Model used for phase inference, at time $t-1$, t and $t+1$. Bold arrows correspond to state transitions, while light arrow correspond to state emissions.

1.2 Parameters of the model

In all analyses, the number of states for the phase, N, and for the O-U processes, M, were taken as $N = 48$ and $M = 30$, yielding a total number of discrete states of 43200.

1.2.1 Parameters common to dividing and non-dividing cells

We first discuss the parameters describing the circadian oscillations in individual cells, which we assume as independent from the coupling with the cell cycle. These parameters concern the oscillator period, phase noise, amplitude and background processes, as well as the experimental noise. The parameters were estimated as described below, and are given in Table 1 for both NIH3T3 and U2OS cells. Since the estimates were found to be very similar at the three experimental temperatures, we considered fixed (temperature-independent) values.

	$T_\theta(h)$	$\sigma_\theta(rad.h^{-1/2})$	μ_A	σ_A	μ_B	σ_B	$\gamma_A(h^{-1})$	$\gamma_B(h^{-1})$	σ_e
NIH3T3	24	0.16	-0.28	0.11	0.08	0.05	0.075	0.075	0.15
U2OS	24	0.18	-0.45	0.15	0.06	0.05	0.075	0.075	0.15

Table 1: Set of parameters for the single cell circadian oscillators in NIH3T3 and U2OS cells. The values of σ_A, σ_B and σ_e are in units of the centered and rescaled signals, see section 1.1.3

The circadian oscillator period T_θ was estimated by averaging the peak to peak times in Rev-Erbα-YFP signals on the whole set of non-dividing traces. The resulting value was 24.28h (NIH3T3, whole dataset), rounded for convenience.

To estimate the phase noise σ_θ, we used the property that the peak-to-peak time distribution of the circadian phase (modeled as a diffusion-drift process) θ obeys:

$$T_{2\pi} \sim IG(\mu = \frac{2\pi}{\omega_\theta} = T_\theta, \lambda = \frac{(2\pi)^2}{\sigma_\theta^2}), \tag{11}$$

where $IG(\lambda, \mu)$ stands for the inverse Gaussian distribution with mean μ and shape parameter λ. This distribution has variance μ^3/λ. Therefore:

$$\sigma_\theta^2 = \frac{Var[T_{2\pi}]4\pi^2}{T_\theta^3} . \tag{12}$$

This expression was used in the NIH3T3 cells. Because we observed only very few non-dividing U2OS cells, we needed to estimate σ_θ from the dividing traces. Since we observed from traces generated *in silico* that the cell-cycle coupling added about 35% of variability in the peak-to-peak distribution, we corrected the value of σ_θ obtained from dividing U2OS cells for this effect.

The means and noise of the O-U processes were estimated from the set of all minima and maxima of the non-dividing traces. More precisely, the mean background was calculated as the average minimum value of the signal, and the mean log amplitude as the average log difference between the maxima and surrounding minima. Similarly, the noise strengths were obtained from the variances of those quantities, using the relationship for the stationary variances: $\sigma_X^2 = 2\gamma_X^2 Var[X]$, for $X = A, B$.

We assumed that the time constants of the A and B processes were slower than the phase fluctuations occurring within one oscillatory cycle, and therefore chose $\gamma_A = \gamma_B = 1/14h^{-1}$. We verified that values of γ_A and γ_B in the range of $1/5h^{-1}$ to $1/30h^{-1}$ did not lead to major differences in the resulting coupling function.

The noise parameter σ_e was set to 0.15. Since the signals were quantile normalized (see section 1.1.3), this corresponds to a relative error of about 15%.

1.2.2 Parameters of the coupling function

1.2.2.1 The EM algorithm

Here we introduce the expectation-maximization (E-M) algorithm, which will be used to estimate the coupling function.

Denote the sequence of observations by $\mathbf{O}$, the state space by $\boldsymbol{\mathcal{X}}$, a given sequence of states by $\mathbf{X}$ and the current and updated set of parameters by $\boldsymbol{\Lambda}'$ and $\boldsymbol{\Lambda}$, respectively. The Q function of the EM [4] is written:

$$Q(\boldsymbol{\Lambda}, \boldsymbol{\Lambda}') = \sum_{\mathbf{X} \in \boldsymbol{\mathcal{X}}} \log(p(\mathbf{O}, \mathbf{X}|\boldsymbol{\Lambda}))p(\mathbf{X}|\mathbf{O}, \boldsymbol{\Lambda}') . \tag{13}$$

Here, the sequence $\mathbf{X}$ is composed of states $\mathbf{x}$ such that $\mathbf{X} = \{\mathbf{x}_1, ..., \mathbf{x}_t, ..., \mathbf{x}_T\}$, and these states are themselves composed of three substates for the phase, the amplitude and the background: $\mathbf{x} = (\psi, a, b)$. In our problem, if we define i_0 as the index associated with the

first state of the sequence $\boldsymbol{X}$, the probability of the observations and the states can be written as a product:

$$p(\mathbf{O}, \boldsymbol{X}|\boldsymbol{\Lambda}) = \boldsymbol{\pi}_{i_0} \prod_{t=1}^{T} p(\boldsymbol{X}_{t+1}|\boldsymbol{X}_t, \boldsymbol{\Lambda}) p(O_{t+1}|\boldsymbol{X}_{t+1}, \boldsymbol{\Lambda}) . \tag{14}$$

This equation enables to rewrite the function Q as three separated sums:

$$
\begin{aligned}
Q(\boldsymbol{\Lambda}, \boldsymbol{\Lambda}') = \sum_{\mathbf{X} \in \boldsymbol{\mathcal{X}}} \log(\boldsymbol{\pi}_{i_0}) p(\boldsymbol{X}|\mathbf{O}, \boldsymbol{\Lambda}') &+ \sum_{\mathbf{X} \in \boldsymbol{\mathcal{X}}} \left(\sum_{t=1}^{T} \log(p(\boldsymbol{X}_{t+1}|\boldsymbol{X}_t, \boldsymbol{\Lambda})) \right) p(\boldsymbol{X}|\mathbf{O}, \boldsymbol{\Lambda}') \\
&+ \sum_{\mathbf{X} \in \boldsymbol{\mathcal{X}}} \left(\sum_{t=1}^{T} \log(p(O_{t+1}|\boldsymbol{X}_{t+1}, \boldsymbol{\Lambda})) \right) p(\boldsymbol{X}|\mathbf{O}, \boldsymbol{\Lambda}') .
\end{aligned}
\tag{15}
$$

This expression readily extends to several traces by adding another sum over the trace indices. Each term can now be optimized individually, enabling to find the optimal set of parameters for the initial condition, the state transitions (which contain the coupling function), and the emissions (cf. 1.1.4).

1.2.2.2 Estimation of the initial condition

Taking the derivative of the first term in Eq (15)with respect to the components of $\boldsymbol{\pi}$ leads to the optimal initial condition:

$$\boldsymbol{\pi}_i = p(\boldsymbol{X}_0 = \mathbf{x}_i|\mathbf{O}, \boldsymbol{\Lambda}') \tag{16}$$

1.2.2.3 Estimation of the coupling function

The coupling function is parameterized on a grid of N^2 parameters, such that F_{ij} corresponds to the coupling for the pair of phases $(\theta_i, \phi_j) \in \boldsymbol{\Psi}^2$. Due to this high number of parameters, regularization constraints were added. Specifically, the squared norm of the gradient, $||\nabla F_{ij}||^2 = (\frac{F_{i+1,j} - F_{i,j}}{\Delta \psi})^2 + (\frac{F_{i,j+1} - F_{i,j}}{\Delta \psi})^2$ is used to control for smoothness. In addition, we controlled the sparseness of the coupling function using the squared norm. The penalized version of Q is therefore:

$$Q_p(\boldsymbol{\Lambda}, \boldsymbol{\Lambda}') = Q(\boldsymbol{\Lambda}, \boldsymbol{\Lambda}') - \lambda_1 \sum_{i,j} ||\nabla F_{ij}||^2 - \lambda_2 \sum_{i,j} F_{ij}{}^2 \tag{17}$$

Starting again from Eq. (15) augmented with these new penalization terms yields:

$$
\begin{aligned}
\frac{\partial Q_p(\boldsymbol{\Lambda}, \boldsymbol{\Lambda}')}{\partial F_{kl}} = \overbrace{\frac{\partial}{\partial F_{kl}} \left[\sum_{\mathbf{X} \in \boldsymbol{\mathcal{X}}} \left(\sum_t \log(p(\boldsymbol{X}_{t+1}|\boldsymbol{X}_t, \boldsymbol{\Lambda})) \right) p(\boldsymbol{X}|\mathbf{O}, \boldsymbol{\Lambda}') \right]}^{E_1} \\
\underbrace{- \frac{\partial}{\partial F_{kl}} \left[\lambda_1 \sum_{i,j} ||\nabla F_{ij}||^2 + \lambda_2 \sum_{i,j} F_{ij}^2 \right]}_{E_2}
\end{aligned}
\tag{18}
$$

13

The first part of this equation, E_1, corresponds to the state transitions, while the second part, E_2, corresponds to the penalization. Equating this to zero to find the maxima conditions, and explicitly taking the sequence of cell-cycle states into account, we obtain:

$$
\frac{\partial}{\partial F_{kl}} \left[\sum_{i_1,i_2} \sum_{j_1,j_2} \sum_{k_1,k_2} \sum_{t} \log(p(\theta_{i_2}, a_{j_2}, b_{k_2} | \theta_{i_1}, \phi_t, a_{j_1}, b_{k_1}, \boldsymbol{\Lambda})) \right.
$$
$$
\left. p(\mathbf{x}_t = (\theta_{i_1}, a_{j_1}, b_{k_1}), \mathbf{x}_{t+1} = (\theta_{i_2}, a_{j_2}, b_{k_2}) | \mathbf{O}, \boldsymbol{\Lambda}') \right] = E_2 \tag{19}
$$

Note here that $\theta_{i_1}, \theta_{i_2}, a_{j_1}, a_{j_2}, b_{k_1}, b_{k_2}$ are hidden states, for which we infer a distribution of probability with the HMM, while ϕ_t is given as an external parameter. Now, the Markov propagators for the phase, amplitude and background being independent (cf. eq. 8), we have:

$$
\log\left(p(\theta_{i_2}, a_{j_2}, b_{k_2} | \theta_{i_1}, \phi_t, a_{j_1}, b_{k_1}, \boldsymbol{\Lambda})\right)) = \log\left(p(\theta_{i_2} | \theta_{i_1}, \phi_t, \boldsymbol{\Lambda})\right)
$$
$$
+ \log\left(p(a_{j_2} | a_{j_1}, \boldsymbol{\Lambda})\right) + \log\left(p(b_{k_2} | b_{k_1}, \boldsymbol{\Lambda})\right) \tag{20}
$$

Since the transitions probabilities for the amplitude and the background do not depend on the coupling function, they cancel out with the derivative. The remaining sum leads to the marginal joint distribution of phases at time t and $t+1$. To keep continuity with the previous notation, we denote the marginal $p(\theta_t = \theta_i) = \sum_{\theta_i, a_j, b_k} p(\mathbf{x}_t = (\theta_i, a_j, b_k))$ by $p(\mathbf{x}_t = (\theta_i, ., .))$.

We therefore have:

$$
\frac{\partial}{\partial F_{kl}} \left[\sum_{i_1,i_2} \sum_{t} \log\left(p(\theta_{i_2} | \theta_{i_1}, \phi_t, \boldsymbol{\Lambda})\right) p(\mathbf{x}_t = (\theta_{i_1}, ., .), \mathbf{x}_{t+1} = (\theta_{i_2}, ., .) | \mathbf{O}, \boldsymbol{\Lambda}') \right] = E_2 \tag{21}
$$

Now, $p(\mathbf{x}_t = (\theta_{i_1}, ., .), \mathbf{x}_{t+1} = (\theta_{i_2}, ., .) | \mathbf{O}, \boldsymbol{\Lambda}')$ doesn't depend on the new coupling function parameters F_{kl}, so it can be treated as a multiplicative constant. Defining $\omega_\theta = 2\pi/T_\theta$, this yields:

$$
\frac{\partial}{\partial F_{kl}} \left[\sum_{i_1,i_2} \sum_{t} \log \left(\frac{1}{\sigma_\theta \sqrt{2\pi dt}} e^{-\frac{1}{2}\left(\frac{\theta_{i_2} - (\theta_{i_1} + \omega_\theta dt + F(\theta_{i_1}, \phi_t) dt)}{\sigma_\theta^2 dt} \right)^2} \right) \right.
$$
$$
\left. p(\mathbf{x}_t = (\theta_{i_1}, ., .), \mathbf{x}_{t+1} = (\theta_{i_2}, ., .) | \mathbf{O}, \boldsymbol{\Lambda}') \right] = E_2 \tag{22}
$$

All the terms that do not depend on $F_{kl} = F(\theta_k, \phi_l)$ are removed by the derivative, which simplifies to:

$$
\sum_{i_2} \sum_{\{t | \phi_t = \phi_l\}} \frac{\theta_{i_2} - (\theta_k + \omega_\theta dt + F_{kl} dt)}{\sigma_\theta^2} p(\mathbf{x}_t = (\theta_k, ., .), \mathbf{x}_{t+1} = (\theta_{i_2}, ., .) | \mathbf{O}, \boldsymbol{\Lambda}') = E_2 \tag{23}
$$

F_{kl} can now be isolated, and we can sum over θ_{i_2} in the denominator:

14

$$F_{kl} = \frac{-\sigma_\theta^2 E_2 + \sum_{i_2} \sum_{\{t|\phi_t=\phi_l\}} (\theta_{i_2} - (\theta_k + \omega_\theta dt)) \, p(\mathbf{x}_t = (\theta_k, ., .), \mathbf{x}_{t+1} = (\theta_{i_2}, ., .)|\mathbf{O}, \mathbf{\Lambda}')}{dt \sum_{\{t|\phi_t=\phi_l\}} p(\mathbf{x}_t = (\theta_k, ., .)|\mathbf{O}, \mathbf{\Lambda}')} \tag{24}$$

Note that the function $w(\theta)$ is involved non-explicitly in this equation, through the computation of the posterior phase distributions. From eq. 18, we find:

$$E_2 = \frac{\partial}{\partial F_{kl}} \left[\lambda_1 \sum_{i,j} (\frac{F_{i+1,j} - F_{i,j}}{\Delta\psi})^2 + (\frac{F_{i,j+1} - F_{i,j}}{\Delta\psi})^2 + \lambda_2 \sum_{i,j} F_{ij}^2 \right] \tag{25}$$

Taking the derivative, and re-injecting into Eq. 24 yields:

$$\begin{aligned}
F_{kl} & \left[dt \sum_{\{t|\phi_t=\phi_l\}} p(\mathbf{x}_t = (\theta_k, ., .)|\mathbf{O}, \mathbf{\Lambda}') + \frac{8\lambda_1\sigma_\theta^2}{\Delta\psi^2} + 2\lambda_2\sigma_\theta^2 \right] \\
& - \frac{2\lambda_1\sigma_\theta^2}{\Delta\psi^2} F_{k-1,l} - \frac{2\lambda_1\sigma_\theta^2}{\Delta\psi^2} F_{k+1,l} - \frac{2\lambda_1\sigma_\theta^2}{\Delta\psi^2} F_{k,l+1} - \frac{2\lambda_1\sigma_\theta^2}{\Delta\psi^2} F_{k,l-1} \\
& = \sum_{i_2} \sum_{\{t|\phi_t=\phi_l\}} (\theta_{i_2} - (\theta_k + \omega_\theta dt)) \, p(\mathbf{x}_t = (\theta_k, ., .), \mathbf{x}_{t+1} = (\theta_{i_2}, ., .)|\mathbf{O}, \mathbf{\Lambda}')
\end{aligned} \tag{26}$$

For readability, we define the new following quantities:

$$\begin{cases}
Q_1 = dt \sum_{\{t|\phi_t=\phi_l\}} p(\mathbf{x}_t = (\theta_k, ., .)|\mathbf{O}, \mathbf{\Lambda}') + \frac{8\lambda_1\sigma_\theta^2}{\Delta\psi^2} + 2\lambda_2\sigma_\theta^2 \\
Q_2 = -\frac{2\lambda_1\sigma_\theta^2}{\Delta\psi^2} \\
Q_{k,l} = \sum_{i_2} \sum_{\{t|\phi_t=\phi_l\}} (\theta_{i_2} - (\theta_k + \omega_\theta dt)) \, p(\mathbf{x}_t = (\theta_k, ., .), \mathbf{x}_{t+1} = (\theta_{i_2}, ., .)|\mathbf{O}, \mathbf{\Lambda}')
\end{cases} \tag{27}$$

This gives:

$$F_{kl}Q_1 + (F_{k-1,l} + F_{k+1,l} + F_{k,l-1} + F_{k,l+1})Q_2 = Q_{k,l} \tag{28}$$

This is a linear equation for F_{kl}. Since Eq. 26 holds $\forall k, l \in \mathbb{N}^2$, this can be rewritten as:

$$\mathbf{Ax} = \mathbf{b} \tag{29}$$

Where $\mathbf{A}$ is a matrix containing the Q_1 and Q_2 terms, $\mathbf{x}$ is the vector containing the F_{kl} terms and $\mathbf{b}$ the vector containing the $Q_{k,l}$ terms. Due to the regularization, Q_1 is always invertible.

1.2.2.4 Regularization

λ_1 is found using four-fold cross-validation, *i.e.* by splitting the NIH3T3 dataset into four chunks and scanning which λ_1 value gives the best generalization, *i.e.* maximizes the likelihood of the left-out test traces. The resulting value is 10^{-6}.

The value of λ_2 is set according to the following principle. The update expression for the coupling function (when $\lambda_1 = 0$) reads:

$$F_{kl} = \frac{\sum_{i_2} \sum_{\{t|\phi_t=\phi_l\}} (\theta_{i_2} - (\theta_k + \omega_\theta dt)) \, p(\mathbf{x}_t = (\theta_k,.,.), \mathbf{x}_{t+1} = (\theta_{i_2},.,.)|\mathbf{O}, \boldsymbol{\Lambda}')}{2\sigma_\theta^2 \lambda_2 + dt \sum_{\{t|\phi_t=\phi_l\}} p(\mathbf{x}_t = (\theta_k,.,.)|\mathbf{O}, \boldsymbol{\Lambda}')} \tag{30}$$

Thus, λ_2 buffers the sum $dt \sum_{\{t|\phi_t=\phi_l\}} p(\mathbf{x}_t = (\theta_k,.,.)|\mathbf{O}, \boldsymbol{\Lambda}')$, especially when the latter is small, *i.e.* for the phase-space points which are rarely visited by the cells. Defining T as the total number of time measurements (from all cells), we set:

$$\lambda_2 = \frac{T\lambda_2'}{2\sigma_\theta^2} dt \ . \tag{31}$$

The interpretation is as follow: given a phase-space state that is visited once in T time points, if $\lambda_2' = \frac{1}{T}$ then the corresponding coupling parameter is halved. More visited states lead to more robust coupling parameters, and conversely for less visited states.

In practice, we want to be able to interpret λ_2' independently of the total number of time points, and we therefore compute it in units of cell-cycle periods, such that the coupling parameter of a state visited once every 200 cell-cycles is halved, that is:

$$\lambda_2' = \frac{1}{200 T_\phi} \tag{32}$$

1.3   Assessment of model assumptions

In our model for the signal $S_t = \exp(A_t)w(\theta_t) + B_t + \xi$, we assumed that the dynamics of the amplitude, background and phase variables A_t, B_t and θ_t were uncoupled. Within our probabilistic framework, we can *a posteriori* verify this hypothesis, by analyzing the joint posterior distribution $P(\theta_t, A_t, B_t|\mathbf{O})$. Indeed, we can compute the expected values of the three latent variables corresponding to each measured observation O_t as follows:

$$\begin{cases} \mathbb{E}[\theta_t] = \arg(\sum_{i,j,k} p(\theta_t = \theta_i, A_t = a_j, B_t = b_k|\mathbf{O})e^{i\theta_i}) \\ \mathbb{E}[A_t] = \sum_{i,j,k} p(\theta_t = \theta_i, A_t = a_j, B_t = b_k|\mathbf{O})a_j \\ \mathbb{E}[B_t] = \sum_{i,j,k} p(\theta_t = \theta_i, A_t = a_j, B_t = b_k|\mathbf{O})b_k \end{cases} \tag{33}$$

As shown in Fig. 8, both the expected amplitudes and backgrounds are on average only weakly dependent on the expected phases. Indeed, the means for A and B vary by, respectively, less than $\pm 10\%$ and $\pm 20\%$ compared to the global means. In fact, the variation in the means of these expected values in function of the phases is much lower than the spread observed in the phase bins (corresponding to the many measurements with the same expected phases).
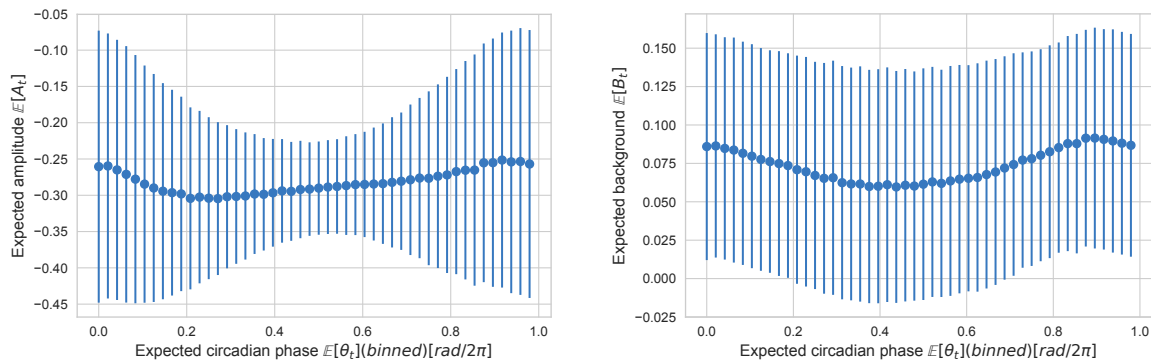
Figure 8: Expected value of the amplitude A_t (**left**) and background B_t (**right**) in function of the expected circadian phase θ_t (binned). The data show the means (dots) and standard deviations computed over all the NIH3T3 cell traces, all temperature included.

Similarly, we then analyzed the (a posteriori) estimated phase noise σ_θ in function of the circadian phase θ_t. To do this, we compute a phase-dependent estimate of σ_θ:

$$\sigma_\theta^2(\theta_i) = \frac{\sum_{j,k,t} \left(\theta_k - (\theta_i + (\omega_\theta + F(\theta_i, \phi_j)dt))\right)^2 p(\theta_t = \theta_i, \theta_{t+1} = \theta_k | \phi_t = \phi_j, \mathbf{O})}{dt \sum_{j,k,t} p(\theta_t = \theta_i, \theta_{t+1} = \theta_k | \phi_t = \phi_j, \mathbf{O})} \tag{34}$$

Results (Fig. 9, left) reveal only very weak dependence of σ_θ^2 over the circadian phase θ. Indeed, the means in σ_θ vary from 0.016 to 0.017, *i.e.* a deviation of about $\pm 6\%$.

Finally, we analyzed the measurement noise ξ. We thus computed the prediction of the model y_t as $y_t = \exp(\mathbb{E}[A_t])w(\mathbb{E}[\theta_t]) + \mathbb{E}[B_t]$, and analyzed the distributions of residuals $y_t - O_t$ binned by expected circadian phase (Fig. 9, right). Here, we find that the residuals are centered on 0 within a good approximation (± 0.035), showing that there is no systematic bias in the noise model.
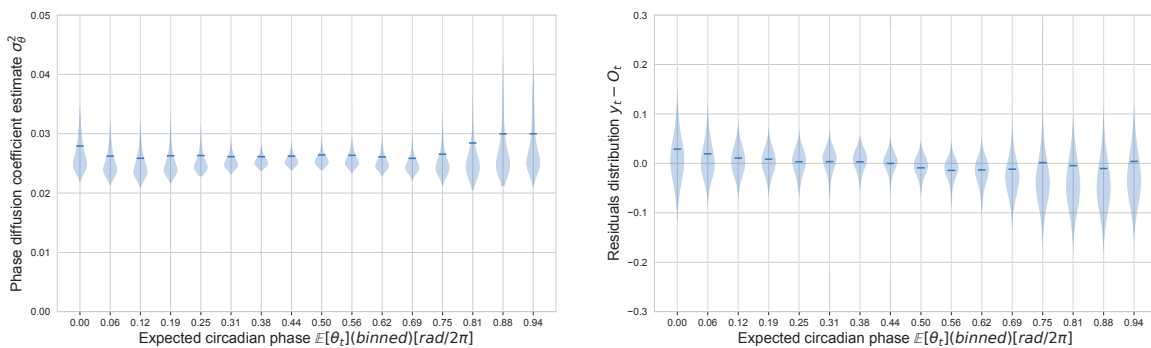

Figure 9: **Left**: Evolution of the distribution of phase diffusion coefficient estimates σ_θ^2 with the expected circadian phase θ_t (binned). **Right**: Evolution of the distribution of residuals $y_t - O_t$ with the expected circadian phase θ_t (binned). Dark horizontal dashes indicate the means. The computation are made from the distributions computed on all the traces coming from NIH3T3 cells, all temperature included.

1.4 Assessment of the parameter estimation

To assess the parameter estimation, we simulated traces *in silico* and re-estimated the parameters using the same methods as for the experimental traces. The generated traces were of the same scale and length as the experimental traces. The regression parameters γ_A, γ_B and the noise parameters σ_e were taken from Table 1.

Table 2 summarizes the results for all estimated parameters. Although we expect some imprecisions due to the stochasticity of the system, the relative error remains low for every parameter.

	$T_\theta(h)$	$\sigma_\theta(rad.h^{-1/2})$	μ_A	σ_A	μ_B	σ_B
Simulated	24.0	0.16	-0.28	0.11	0.08	0.05
Estimated	24.0	0.16	-0.24	0.11	0.04	0.05

Table 2: Simulated and estimated model parameters.

For the reliability of the estimated coupling function, we refer to the main text (Figure S1, panels b and c).

2 Simulations of the dynamical system

2.1 Model

A deterministic model for the phase dynamics is obtained by removing the phase noise term from the full model. In addition, to study the bifurcations (phase locked states) in function of the coupling strength, we added a multiplicative factor for the coupling function called K: ($K = 1$ for the biological coupling value).

$$\begin{cases} \dot{\theta} = \frac{2\pi}{T_\theta} + KF(\theta, \phi) \\ \dot{\phi} = \frac{2\pi}{T_\phi} \end{cases} \tag{35}$$

2.2 Phase-locked states

Weakly coupled oscillators can phase-lock when the ratio of their natural period is close to a ratio of integer numbers, *i.e.* $\frac{T_\theta}{T_\phi} \simeq \frac{p}{q}$ with $p, q \in \mathbb{N}$ [5]. To characterize mode-locked states, we estimate $\bar{\omega}_\theta$, defined as the average circadian phase velocity:

$$\bar{\omega}_\theta = \lim_{t \to \infty} \frac{\theta(t)}{t} . \tag{36}$$

Phase-locking occurs when $\bar{\omega}_\theta$ remain constant within an interval of cell-cycle frequencies ω_ϕ, as represented by Arnold tongue diagrams. Outside of such stable intervals, the dynamics is quasiperiodic.

3 Correspondence between cell-cycle phase and biological cell-cycle events

In our model, we assumed a linear progression of the cell-cycle phase between two successive divisions. To get a better handle on the relation between this measure and cell-cycle events, we generated a set of 104 experimental traces from NIH3T3 cells expressing the FUCCI cell-cycle sensor [9]. To obtain estimates of the boundaries for the different cell-cycle events, we normalized and rescaled all fluorescent signals before mapping them to a 0 to 2π interval (from division to division, Figure 10). Despite biological variability, the growth phase 1 (G1) generally spans from 0 to $0.4 \times 2\pi$ rad, while DNA replication and growth phase 2 (S-G2) usually occur between $0.4 \times 2\pi$ rad and $0.95 \times 2\pi$ rad. Mitosis usually happens from $0.95 \times 2\pi$ rad to 2π rad.
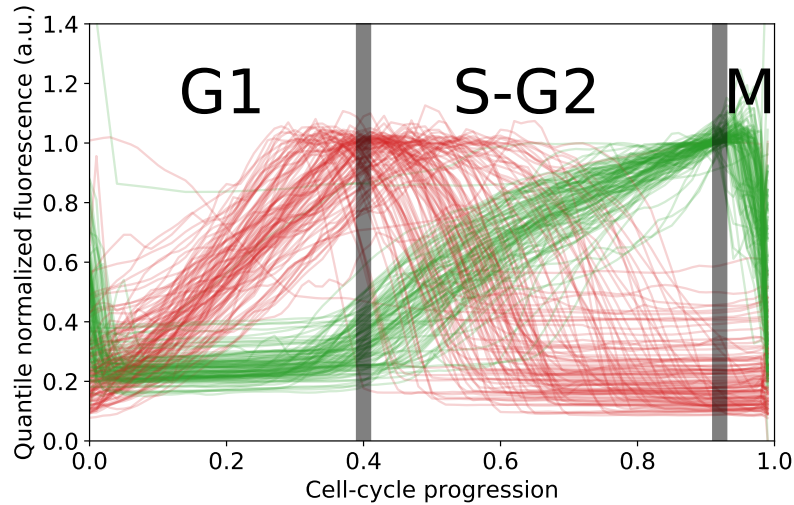

Figure 10: Normalized experimental traces from NIH3T3 cells expressing the FUCCI cell-cycle reporter system enable the association between the physical cell-cycle phase and the biological phase. The red and green fluorescence signals correspond respectively to mKO2-Cdt1 and mAG-Geminin FUCCI reporters. The vertical grey lines denote the (approximate) separation between the different biological cell-cycle phases.

4 Analysis of a population of bioluminescence traces under temperature entrainment
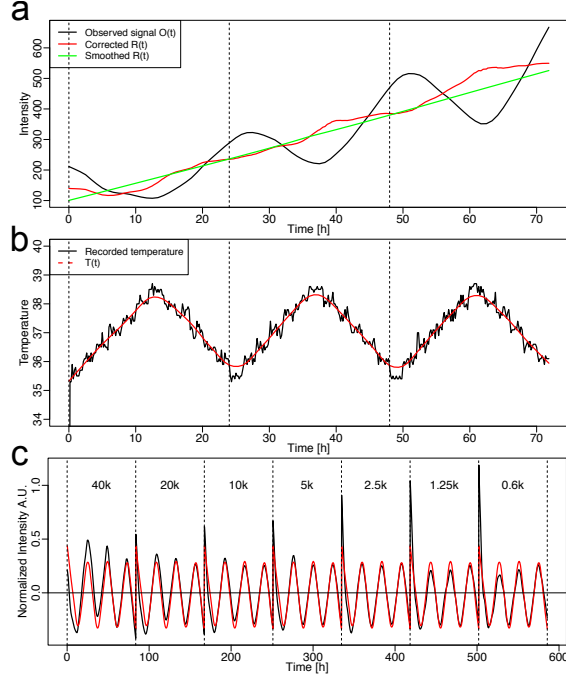

Figure 11: **a:** Observed $O(t)$, smoothed $R(t)$ and corrected $R(t)$ signals obtained from U2OS cells expressing a PGK-luciferase reporter grown at low cell confluence. **b:** Recorded 35.5°C-38.5°C temperature entrainment (black) and smoothed signal (red, $T(t)$) from **a**. **c:** Normalized PGK-Luc signal obtained from U2OS cells grown at different confluences (black) and the optimal fit using $t_d = 80$ min and $k = -0.26$ (red).

The enzymatic activity of luciferase is known to be higher at lower temperature [6]. Since we applied temperature cycles from 35.5°C to 38.5°C for entrainment, even a luciferase reporter driven by a constitutive gene, *e.g. Pgk*, would show an oscillatory signal (Fig. 11, panels a and b)[7, 8]. To correct the signal for this systematic effect, we found that the observed signal $O(t)$ could be well fitted by the following expression

$$O(t) = R(t)(1 + k(T(t - t_d) - T_0) , \qquad (37)$$

where $R(t)$ is the real signal exempts of any temperature artifact, $T(t)$ is the temperature profile, $T_0 = 37$°C), $k =$ is a magnitude coefficient, and t_d minutes a time delay. To determine the free parameters t_d and k, we used the luciferase signal obtained from U2OS cells expressing a PGK luciferase reporter (U2OS-PGK-Luc) which is expected to yield a non-oscillating signal after correction (Fig. 11a). Specifically, we optimized d and k to best fit $O(t)$, after smoothing $O(t)$ to obtain a proxy for $R(t)$. The optimal fit yielded $t_d = 80$ minutes and $k = -0.26$ (Fig. 11c). These values of t_d and k were then used to detrend the circadian luminescence signals using Eq. (37). Importantly, we performed all our luciferase experiments using the Luc2p

luciferase (Promega), a destabilized version of the WT Photinus pyralis luciferase optimized for expression in mammals. Consequently, we could use the optimized t_d and k to retrieve the corrected signal $R(t)$ for all our constructs.

References

[1] Bieler, J., Cannavo, R., Gustafson, K., Gobet, C., Gatfield, D., & Naef, F. (2014). Robust synchronization of coupled circadian and cell cycle oscillators in single mammalian cells. Molecular systems biology, 10(7), 739.

[2] Rabiner, L. R. (1989). A tutorial on hidden Markov models and selected applications in speech recognition. Proceedings of the IEEE, 77(2), 257-286.

[3] Lemons, D. S., & Langevin, P. (2002). An introduction to stochastic processes in physics. JHU Press.

[4] Bilmes, J. A. (1998). A gentle tutorial of the EM algorithm and its application to parameter estimation for Gaussian mixture and hidden Markov models. International Computer Science Institute, 4(510), 126.

[5] Pikovsky, A., Rosenblum, M., Kurths, J., & Kurths, J. (2003). Synchronization: a universal concept in nonlinear sciences (Vol. 12). Cambridge university press.

[6] Koksharov, M.I. and Ugarova, N.N. (2012) Approaches to engineer stability of beetle luciferases. Computational and structural biotechnology journal, 2.

[7] Norrman, K., Fischer, Y., Bonnamy, B., Wolfhagen Sand, F., Ravassard, P. and Semb, H. (2010) Quantitative comparison of constitutive promoters in human ES cells. PloS one, 5.

[8] Qin, J.Y., Zhang, L., Clift, K.L., Hulur, I., Xiang, A.P., Ren, B.Z. and Lahn, B.T. (2010) Systematic comparison of constitutive promoters and the doxycycline-inducible promoter. PloS one, 5.

[9] Sakaue-Sawano, A., Kurokawa, H., Morimura, T., Hanyu, A., Hama, H., Osawa, H., ... & Imamura, T. (2008). Visualizing spatiotemporal dynamics of multicellular cell-cycle progression. Cell, 132(3), 487-498.